

**POLITECNICO**  
**MILANO 1863**

# **Project report for Machine Design**

by

Alessio Panzeri (10766979)

Edoardo Stello (10796942)

Mantas Kazėnas (11076681)

Alessandro Zaniboni (10781938)

Academic Year: 2024–2025

Course: Machine Design

Professors: Andrea Manes, Salvatore Annunziata

Politecnico di Milano

June 19, 2025

# Glossary

**FEM** Finite Element Method: numerical technique for approximating solutions in structural mechanics.

**SHM** Structural Health Monitoring: real-time evaluation system for detecting damage or degradation in structures.

**UTS** Ultimate Tensile Strength: the maximum stress a material can withstand while being stretched.

**MRGB** Main Rotor Gearbox: gearbox transferring power from the engine to the helicopter's main rotor.

**DIC** Digital Image Correlation: a non-contact optical method that measures full-field surface strain and displacement by tracking patterns on the specimen surface.

**VM** Von Mises: refers to the Von Mises yield criterion, which is used to determine whether a given stress state will cause material yielding under complex loading.

**SIMP** Solid Isotropic Material with Penalization: an algorithm used in topology optimization to find the best distribution of material within a design space to minimize weight while maintaining stiffness.

$A_{net}$  Cross-sectional (resistant) area [mm<sup>2</sup>]

$d, D, D_{int}, D_{ext}$  diameters, internal and external diameters [mm]

$r$  Radius [mm]

$R$  Mohr circle radius [MPa]

$t$  Thickness [mm] or time [s]

$l$  Length [mm]

$L_{cr}$  Eulerian critical length for buckling [mm]

$\omega$  Angular velocity [rad/s]

$N$  Axial force [N]

$T$  Shear force [N]

$M$  Bending moment [N·m]

$M_t$  Torsional moment [N·m]

$\sigma$  Normal stress [MPa]

$\tau$  Shear stress [MPa]

$\varepsilon$  Strain (dimensionless)

$E$  Young's modulus [MPa]

$G$  Shear modulus [MPa]

$\nu$  Poisson's ratio (dimensionless)

$\sigma^y$  Yield strength [MPa]

$\sigma_{uts}$  Ultimate tensile strength [MPa]

$\sigma_{FA,a}$  Endurance limit under alternate loading [MPa]

$\sigma^*$  Equivalent stress (e.g., Sines or Von Mises) [MPa]

$\sigma_{adm}$  Admissible stress [MPa]

$\sigma_a$  Alternating stress component [MPa]

$\sigma_m$  Mean stress component [MPa]

$\sigma_I, \sigma_{II}, \sigma_{III}$  Principal stress components [MPa]

$\sigma_{a,lim}$  New Alternate fatigue limit [MPa]

$\sigma_{m,lim}$  New Mean fatigue limit [MPa]

$\rho$  Notch sensitivity factor

$K_t$  Theoretical stress concentration factor

$K_{t,N}$  Axial stress concentration factor

$K_{t,M}$  Bending stress concentration factor

$K_{t,M_t}$  Torsional stress concentration factor

$K_f$  Fatigue notch factor

$m_s$  Surface finish factor

$m_d$  Size (dimension) factor

$q$  Notch sensitivity coefficient

$\eta_i$  Safety factor (general)

$P_{\text{cr}}$  Eulerian critical load [N]

$J$  Torsional constant or polar moment of inertia [mm<sup>4</sup>]

$J_x, J_y$  Second moment of area about x/y axis [mm<sup>4</sup>]

$I_{1,m}$  First stress invariant of the mean stress tensor [MPa]

$EJ$  Bending stiffness [N·m<sup>2</sup>]

# Brief Description

The project focuses on the structural assessment of a helicopter main rotor shaft, or mast. The goal is to evaluate its behavior under static and fatigue loads using analytical methods, finite element simulations (FEM), and experimental data.

Initially, a simplified static analysis was performed based on axial loads, torsion, bending moments, and shear forces. Special attention was paid to identifying the critical section and the main stress components. The mast's static strength was verified using mechanical criteria aligned with material properties.

Two materials, 9310 VAR and 32CDV13, were considered throughout the study. This allowed a direct comparison in terms of strength, fatigue resistance, and overall performance. The dual-material approach helped identify the advantages and limitations of each alloy under identical load conditions.

Next, a detailed analysis was carried out on a physical specimen representative of the mast. Both static and fatigue behaviors were examined, including principal stresses, equivalent stress states, and potential failure zones based on geometry and load distribution.

Analytical results were then compared with FEM simulations and experimental strain data collected through strain gauge rosettes. This multi-method validation confirmed the consistency and reliability of the models used.

The project concludes that the mast design meets the required structural safety margins under the specified load cases. The integration of analytical modeling, FEM, and experimental validation offered a comprehensive understanding of the mast's structural performance. The work highlights the importance of combining multiple assessment approaches in the design and verification of mechanical components for aerospace applications.

# Index

## Contents

<b>Glossary</b>	<b>1</b>
<b>Brief Description</b>	<b>4</b>
<b>Index</b>	<b>5</b>
<b>1 Introduction</b>	<b>6</b>
<b>2 Body of the Report</b>	<b>9</b>
2.1 State of the Art / Literature Survey . . . . .	9
2.2 Methods . . . . .	10
2.2.1 Static Assessment . . . . .	10
2.2.2 Fatigue Assessment . . . . .	15
2.3 Application to the Specific Case . . . . .	18
2.3.1 Material Properties . . . . .	19
2.3.2 Static Assessment of the Mast – Results . . . . .	19
2.3.3 Static Assessment of the Specimen – Results . . . . .	21
2.3.4 Fatigue Assessment of the Specimen – Results . . . . .	23
2.3.5 FEM Model and Its Application . . . . .	25
2.4 Results and Discussions . . . . .	28
2.4.1 Comparison between analytical, numerical and experimental results	28
<b>3 Final Conclusions</b>	<b>31</b>
<b>Bibliography</b>	<b>34</b>

# Chapter 1

## Introduction

Helicopter rotor systems are among the most structurally demanding mechanical assemblies in aerospace engineering. At the heart of this system lies the *mast*, a vertical shaft responsible for transmitting both torque and axial load from the engine and transmission system to the main rotor hub. Due to its critical structural role, this element is subjected to a combination of demanding loads (including axial force, torsion, bending moment, and shear force) and to complex stress states, and so it must be carefully designed and verified to ensure flight safety and long-term reliability. The region of maximum structural demand typically coincides with the portion of minimum wall thickness, which also includes geometrical features such as notches. These notches act as stress raisers and must be properly characterized using appropriate stress concentration factors.

### Problem Statement

The structural integrity of the mast is a key aspect of rotorcraft safety. Due to the presence of multiple load components and local geometric discontinuities such as notches and spline interfaces, simplified analytical methods must be verified and supported by numerical and experimental approaches. A direct evaluation of the stress state in the most critical region of the mast is therefore essential.

### Hypotheses and Initial Assumptions

The analysis presented in this report is based on a number of assumptions and simplifications, necessary to make the problem tractable and compatible with the available experimental and computational tools. First, all materials involved—namely 9310 VIM-VAR and 32CDV13 steels—are assumed to behave as **linear elastic and isotropic** in the range of loads considered, which is reasonable given the stress levels are below yield. Their mechanical properties (Young's modulus  $E$ , shear modulus  $G$ , and Poisson's ratio  $\nu$ , respectively) are taken as constants and homogeneous throughout the volume. Notably, the shear modulus  $G$  is used directly as a given property, rather than being derived from  $E$

and  $\nu$ , to account for potential variations due to microstructural effects or manufacturing processes.

The stress evaluation is conducted under the assumption of a **biaxial stress state**, as induced by axial and torsional loading in the test specimen, with shear forces considered negligible for simplification. This assumption is supported by both the FEM model and the experimental test rig, which is designed to apply only axial and torsional loads. The strain state is reconstructed from strain gauge rosettes mounted at critical sections, and stresses are then derived using the constitutive law for isotropic linear elasticity.

In the analytical computations, **stress transformation and principal stress evaluation** are carried out assuming a 2D plane stress condition, suitable for thin-wall sections and justified by the nature of the specimen geometry and loading. Simplified models are used for estimating von Mises and Tresca equivalent stresses, which are then compared with both FEM simulations and experimental data.

Finally, boundary conditions for both the MAST and specimen models are idealized: bearings are considered rigid, and load application points are simplified to reproduce equivalent mechanical effects while ensuring computational efficiency and physical representativeness. These assumptions are consistent with the operative guidelines provided and allow for reliable yet manageable verification of structural integrity.

## Objectives

The aim of the present work is to assess the stress state of the mast and its experimental specimen through a multi-approach structural verification process. The project includes:

- A **simplified static assessment of the mast**, considering axial, shear, torque, and bending loads;
- A **static structural verification of the specimen**, based on the real loads applied during testing (axial load, torque, and bending moment);
- A **fatigue analysis of the specimen**, under cyclic axial and torsional loading conditions;
- A **comparison of the results** obtained via analytical formulations, finite element simulations, and experimental measurements using strain gauge rosettes.

## Methodology Overview

First, the mast is analysed analytically under its complete loading scenario, which includes axial force, shear, torque, and bending moment, in order to identify the most critical region from a static point of view.

Subsequently, a laboratory specimen is designed with the aim of reproducing the same internal stress state observed in the mast, rather than replicating its exact geometry. While the overall shape, dimensions, and load application points of the specimen differ from those of the actual component, its geometry and loading conditions are tailored such that the resulting state of stress in the critical area is equivalent to that of the mast. This approach enables a realistic yet manageable experimental setup, allowing for the practical application of loads, the installation of strain gauges, and a clearer interpretation of results. The specimen serves as a simplified physical model that enables both structural validation and experimental correlation, under controlled and repeatable boundary conditions.

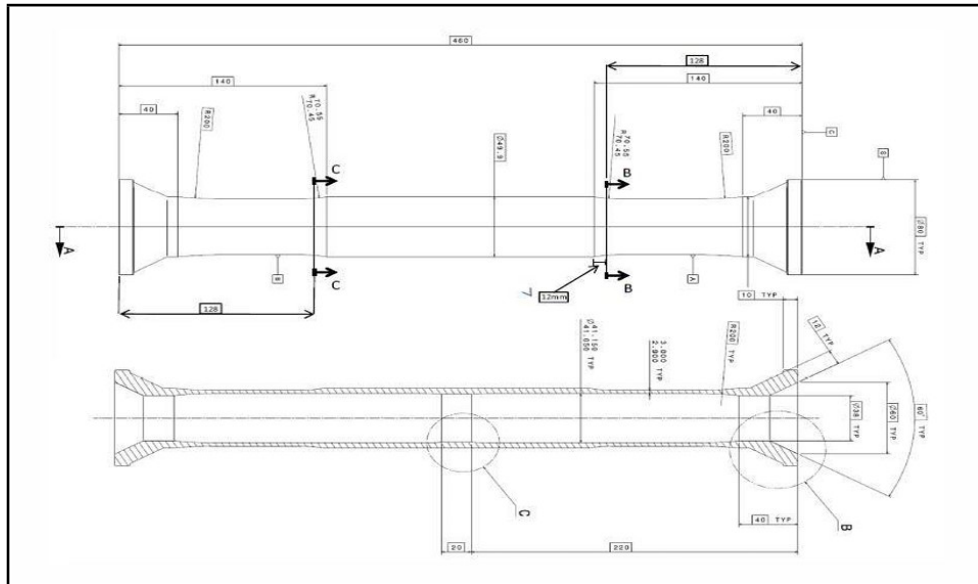


Figure 1.1: Specimen geometry

The specimen is evaluated analytically and through FEM simulations under its test loads, for static analysis, and under alternating/cyclic axial and torsional loads for fatigue assessment.

Finally, experimental strain data from rosette gauges installed on the specimen are processed to reconstruct the local stress state and compared to the results of the previous models. This comparison enables validation of the modelling assumptions and highlights the consistency (or discrepancy) among the three approaches.

# Chapter 2

## Body of the Report

### 2.1 State of the Art / Literature Survey

One of the most critical components in helicopter design, particularly from both structural and kinematic perspectives, is the **mast**. This section reviews its traditional role, structural evolution, and emerging innovations in recent research and applications.

The mast is a vertical structural component that connects the helicopter airframe to the main rotor. It serves as the primary load-bearing and torque-transmitting element, responsible for transferring power and torque from the transmission system to the main rotor. Beyond its role in power transmission, the mast significantly contributes to rotor stiffness and overall stability, directly affecting aerodynamic performance and flight efficiency.

Physically, the mast appears as a hollow cylindrical shaft, manufactured with high geometric precision. It may feature variable diameters along its axis to optimize stress distribution. Internally, it can house concentric shafts or accommodate wiring and hydraulic systems. Its ends are equipped with flanges or tapered joints for connection to the rotor and the transmission.

#### Role

1. **Power Transmission:** The mast transmits the engine-generated torque to the main rotor, ensuring flight performance meets design specifications.
2. **Structural Support:** It withstands static and dynamic loads arising from aerodynamic forces during flight, vibration loads, and maneuver loads.
3. **Alignment and Damping:** By integrating elastic couplings or bearings, the mast helps attenuate vibrations transmitted to the fuselage, enhancing comfort and airframe life.

**4. Interface for Auxiliary Systems:** It accommodates additional components such as hydraulic lines, sensors, and mechanical linkages for blade pitch control.

Historically, helicopter masts have been manufactured from high-strength steel due to its combination of stiffness and durability. More recently, the adoption of titanium alloys and advanced composites has enabled weight reduction and improved fatigue resistance.

Recent research explores technologies such as:

- Hybrid steel-composite mast structures;
- Integration of structural health monitoring (SHM) sensors for real-time monitoring;
- Topological design for shape and mass optimization.

These directions aim to enhance reliability, reduce maintenance costs, and improve flight safety.

An innovative structural and kinematic solution, as implemented in helicopter models such as the MD 500 and MD 600 series, consists of a non-rotating hollow static mast that structurally supports the main rotor at its upper end. This static tube bears the entire lift load in axial tension.

Inside the static mast, a smaller-diameter rotating drive shaft (drive mast) is mounted. It is splined at both ends (to the rotor hub and to the transmission gearbox) but does not carry axial loads. These spline connections allow thermal expansion along the shaft length without generating internal stresses.

This architecture provides several advantages:

- Simplified mechanical interfaces (no axial bearings at rotor or gearbox interfaces);
- Improved reliability of the main rotor gearbox (MRGB), which can use purely radial ball and planetary bearings;
- Accommodation of the tilting swashplate sphere on the external surface of the static mast, simplifying control integration.

In military applications, an additional benefit is the possibility of designing the static mast as a reinforced or bullet-resistant outer shell, enhancing resistance to light ballistic threats and mitigating the risk of rotor detachment, a known critical vulnerability in combat scenarios.

## 2.2 Methods

### 2.2.1 Static Assessment

The static analysis aims to provide a specific characterization of the static strength of a particular component given external loads, geometrical data and constitutive properties

of the material. As first step the equilibrium condition is needed along all 3 cartesian coordinates according to the chosen reference frame:

$$\sum F_x = 0 \quad \sum F_y = 0 \quad \sum F_z = 0 \quad (2.1)$$

$$\sum M_x = 0 \quad \sum M_y = 0 \quad \sum M_z = 0 \quad (2.2)$$

Reaction forces are determined directly by equilibrium equations, depending on the types of boundary conditions.

## Internal forces

Internal forces are calculated following a proper notation which can be summarized by the following schemes:

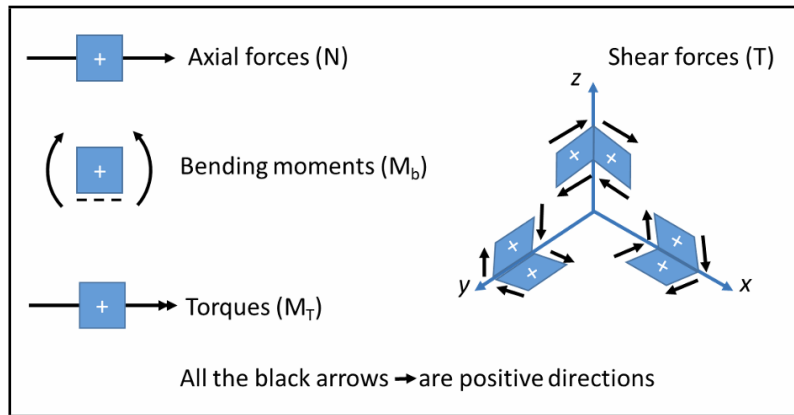


Figure 2.1: Internal Forces Convention

Depending on the type of load condition, "fibers in tension zones" need to be identified to properly state the convention about the internal bending moment of the structure.

## Critical section

The analysis has to be conducted regarding the most critical section of the component, which can be identified by evaluating the most stressed part by means of internal forces contributes along with geometrical considerations (notch effect, smaller diameters etc...).

The critical section of the mast is given as data, instead as for the specimen the critical section has to be determined. No particular points are highlighted through internal forces diagram, ( $N$ ,  $M$ ,  $M_t$  are constant along the structure); so geometrical evaluations are needed. Internal forces are distributed through the structure by means of net area of resistance, the smaller the net area the higher the value of the stress tensor components:

$$\sigma = \frac{F}{A_{net}} \quad (2.3)$$

Using this simple consideration, two identical (by means of geometry) parts of the specimen are highlighted, since internal forces have the same value. The part closest to the clamp boundary condition was chosen for further considerations. The notch effect is the most typical cause for stress increments, in the present case study 2 different notches are identified, each with a different value of radius;  $r_1 = 200\text{mm}$  and  $r_2 = 70\text{mm}$ , respectively, considering as first the one closest to the root of the specimen. The severity of the notch is evaluated using the  $K_t$  parameter, "elastic stress concentration factor", which quantifies the effect of a notch on the stress distribution within a material:

$$K_t = \frac{\sigma_{max}}{\sigma_{nom}} \quad (\text{for uniaxial stress state}) \quad (2.4)$$

$$K_t = \frac{\tau_{max}}{\tau_{nom}} \quad (\text{for torsional stress state}) \quad (2.5)$$

$\sigma_{max}$  and  $\tau_{max}$  identify the local and most critical stress state on which the static analysis is based. Nominal stress values are computed using internal forces evaluation;  $\sigma_{max}$  is computed considering a superposition of effects caused by the axial and bending contributions (given the validity of the De Saint Venant formulation):

$$\sigma = \frac{N}{A} + \frac{M_x}{J_x}y - \frac{M_y}{J_y}x \quad (2.6)$$

$$\sigma_{max_{tot}} = \sigma_{max_N} + \sigma_{max_M} = K_{t_N}\sigma_{nom_N} + K_{t_M}\sigma_{nom_M} \quad (2.7)$$

$K_t$  depends only on the type of load applied and geometrical data, its values are reported in graphs:

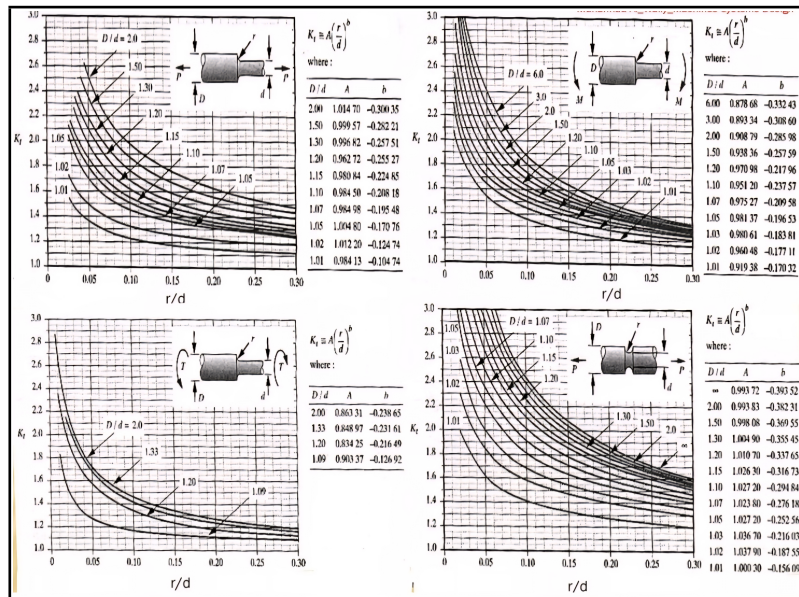


Figure 2.2: Notch Effect Coefficient

As shown in Notch Effect Coefficient for  $r/d \rightarrow +\infty$   $K_t \rightarrow 1$ , the first notch is less severe and can be neglected. An interpolation based on geometrical data of the specimen

and the second notch suggests that the case in question surpasses the validity boundaries of the relation by means of admissible  $r/d$  values; this suggests that also the second notch and its effect by means of peak stress can be neglected; based upon those considerations, for the specimen:

$$K_{t_N} = K_{t_M} = K_{t_{M_t}} = 1 \quad (2.8)$$

The critical section is then chosen as a generic one between 2 notches, since the net resistance area is constant, it is chosen the one closest to the second notch:

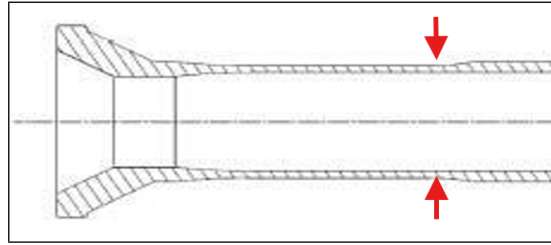


Figure 2.3: Critical Section

### State of stress

The section point of view is chosen as follows:

Be assumed as most critical point the tension portion and a 2D stress state, since shear can be neglected due to the fact that on the extreme point of the section (for a parabolic distribution of  $\tau$  along  $y$ )  $\tau = 0$ . Nominal values of the stress are computed:

$$\sigma_{nom_N} = \frac{N}{\pi \left( \frac{D_e^2}{4} - \frac{D_i^2}{4} \right)} \quad \sigma_{nom_M} = \frac{32MD_e}{\pi(D_e^4 - D_i^4)} \quad \tau_{nom_{M_t}} = \frac{16M_t D_e}{\pi(D_e^4 - D_i^4)} \quad (2.9)$$

Let's consider the effect of possible notches next:

$$\sigma_{max} = K_t \sigma_{nom} \quad \tau_{max} = K_t \tau_{nom} \quad (2.10)$$

$$\sigma_{max_{tot}} = \sigma_{max_N} + \sigma_{max_M} = \sigma_{cr} \quad \tau_{max_{tot}} = \tau_{max} = \tau_{cr} \quad (2.11)$$

### Principal Stresses

To evaluate the principal stress tensor components, Mohr Circles are used:

Each point is identified by  $(\sigma; \tau)$  coordinates, whose sign depends on the coherence with the convention below:

$$P(\sigma_{cr}; \pm \tau_{cr}); \quad Q(0; \pm \tau_{cr}) \quad (2.12)$$

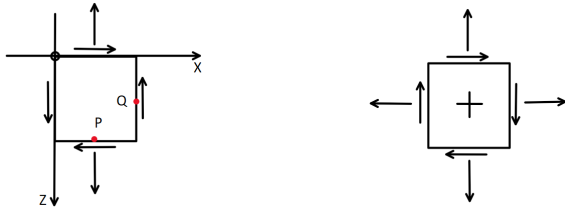


Figure 2.4: Generic State of Stress and Sign Convention

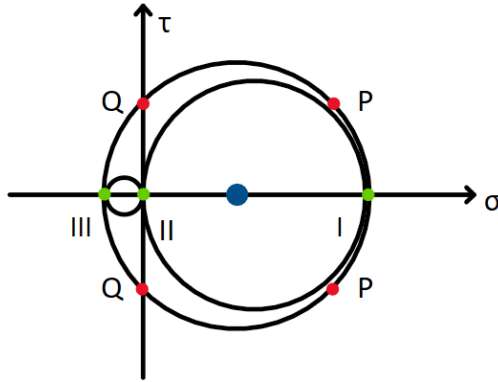


Figure 2.5: Mohr Circles and P. Stresses

$$\begin{cases} \sigma_I = \frac{\sigma_P}{2} + R \\ \sigma_{II} = 0 \\ \sigma_{III} = -R + \frac{\sigma_P}{2} \end{cases} \quad (2.13)$$

### Stress Criteria

To properly assess the strength of the component without any static failure a stress criterion is needed:

$$\sigma^* < \sigma_{adm} = \frac{\sigma^y}{\eta} \quad (\sigma^* \text{ as equivalent stress}) \quad (2.14)$$

Both Guest Tresca and Von Mises are applicable, considering the fact GT is less conservative, VM is used instead:

$$\sigma^* = \sigma_{VM} = \sqrt{\sigma_I^2 + \sigma_{II}^2 + \sigma_{III}^2 - \sigma_I \sigma_{II} - \sigma_{II} \sigma_{III} - \sigma_I \sigma_{III}} \quad (2.15)$$

The safety coefficient is determined for each type of material ,(1 & 2); verifying that is above 1:

$$\eta_1 = \frac{\sigma_1^y}{\sigma^*} \quad \eta_2 = \frac{\sigma_2^y}{\sigma^*} \quad (2.16)$$

## 2.2.2 Fatigue Assessment

The Fatigue analysis aims to assess if the specimen is able to withstand cyclical loads without failure. As first requirement the specimen need to be able to bear the maximum reachable static load condition during its fatigue life, for this reason a static assessment is executed as preliminary step.

After static validations, fatigue analysis can be initiated starting from equilibrium, needed along all the axis to evaluate the reaction forces. Given the external load the procedure to compute the reaction forces by the equilibrium equation and the internal forces is the same as what was previously discussed in the Static Assessment, (as well as the convention).

### Stress Tensors and Principal Component variation in Time

The specimen is subjected to both a constant torque moment and a axial load composed by a constant and a variational part with sinusoidal law in time.

$$N = N_m + N_0 \sin(\omega t) \quad M_z = M_{zm} \quad (2.17)$$

The stress state is represented by a  $[\sigma]$  that is sum of a mean contribution  $[\sigma_m]$  and an alternate one  $[\sigma_a]$ , respectively generated by:

$$[\sigma_m] \rightarrow \sigma_{nom,m}(N_m) \quad \& \quad \tau_{nom,m}(M_{zm}) \quad (2.18)$$

$$[\sigma_a] \rightarrow \sigma_a(N_a = N_0 \sin(\omega t)) \quad (2.19)$$

Each of the stress tensors can be expressed using its principal components:

$$[\sigma_m] = \begin{bmatrix} \sigma_I^m & 0 & 0 \\ 0 & \sigma_{II}^m & 0 \\ 0 & 0 & \sigma_{III}^m \end{bmatrix} \quad [\sigma_a] = \begin{bmatrix} \sigma_{I,a} & 0 & 0 \\ 0 & \sigma_{II,a} & 0 \\ 0 & 0 & \sigma_{III,a} \end{bmatrix} \quad (2.20)$$

Mean principal components are evaluated as in the static assessment. A 2D state of stress is considered, (as superposition of the axial ( $\sigma$ ) and torsion ( $\tau$ ) contribution).

The alternate contribution can be represented as a uniaxial stress state by the stress tensor  $[\sigma_a(t)]$  as follows:

$$[\sigma_a(t)] = \begin{bmatrix} 0 & 0 & 0 \\ 0 & 0 & 0 \\ 0 & 0 & \sigma_{zz,a}(t) \end{bmatrix} \quad \text{where} \quad \sigma_{zz,a} = \frac{N_0 \sin(\omega t)}{\pi \left( \left( \frac{D_e}{2} \right)^2 - \left( \frac{D_i}{2} \right)^2 \right)} \quad (2.21)$$

which principal components  $(\sigma_{I,a}, \sigma_{II,a}, \sigma_{III,a})$  are defined as temporal functions considering the time evolution of  $\sigma_{zz,a}$ ; orthogonal to the  $xy$  plane of the section.

Thanks to the symmetrical properties of the specimen along the (x,y,x) reference frame axis, principal directions coincides with cartesian ones. Following the classical convention when ordering eigenvalues of the stress tensor as its principal components ( $\sigma_I > \sigma_{II} > \sigma_{III}$ ):

$$if \quad \sigma_{zz,a}(t) > 0 \quad \sigma_I(t) = \sigma_{zz,a}(t), \quad \sigma_{II}(t) = 0, \quad \sigma_{III}(t) = 0 \quad (0 < \omega t < \pi) \quad (2.22)$$

$$if \quad \sigma_{zz,a}(t) > 0 \quad \sigma_I(t) = 0, \quad \sigma_{II}(t) = 0, \quad \sigma_{III}(t) = \sigma_{zz,a}(t) \quad (\pi < \omega t < 2\pi) \quad (2.23)$$

## Eulerian Instability

To verify the static stability under compression the following condition needs to be satisfied:

$$|N_{min}| << \frac{P_{cr}}{\eta} \quad \text{where} \quad \left( P_{cr} = \frac{\pi^2 E J}{l^2} \right) \quad (2.24)$$

Considering as  $N_{min}$  the maximum compressive load applied to the structure and as  $P_{cr}$  the "Critical Eulerian Load", which represents the minimum load required to reach instability condition as function of geometrical and constitutive parameters for a specific material. Stability condition has to be verified by a safety factor  $\eta > 3$ .

## Stress Criteria

To properly assess specimen's resistance to fatigue loads Sines Criteria is used:

$$\sigma_a^* \leq \sigma'_{FA,A} \left( 1 - \frac{I_{1,m}}{\sigma^y} \right) \frac{1}{\eta_f} \quad (2.25)$$

Each parameter is determined according to its definition and properties of the specimen.

$$\sigma'_{FA,A} = \frac{\sigma_{FA,A} m_s m_d}{K_f} \quad (2.26)$$

- $\sigma_{FA,A}$  = Standard Fatigue Strength (depends on the material)
- $m_s$  = Surface finish Factor
- $m_d$  = Geometrical Factor (= 1 for axial fatigue)

- $K_f$  = Notch Fatigue Coefficient

$$K_f = 1 + q(K_t - 1) \quad (2.27)$$

Based on consideration made previously in the static assessment a fatigue notch coefficient of  $K_t = 1$  is used. The finishing factor  $m_s$  is evaluated using experimental tables, according to the following manufacturing sequence: turning, milling and filing:

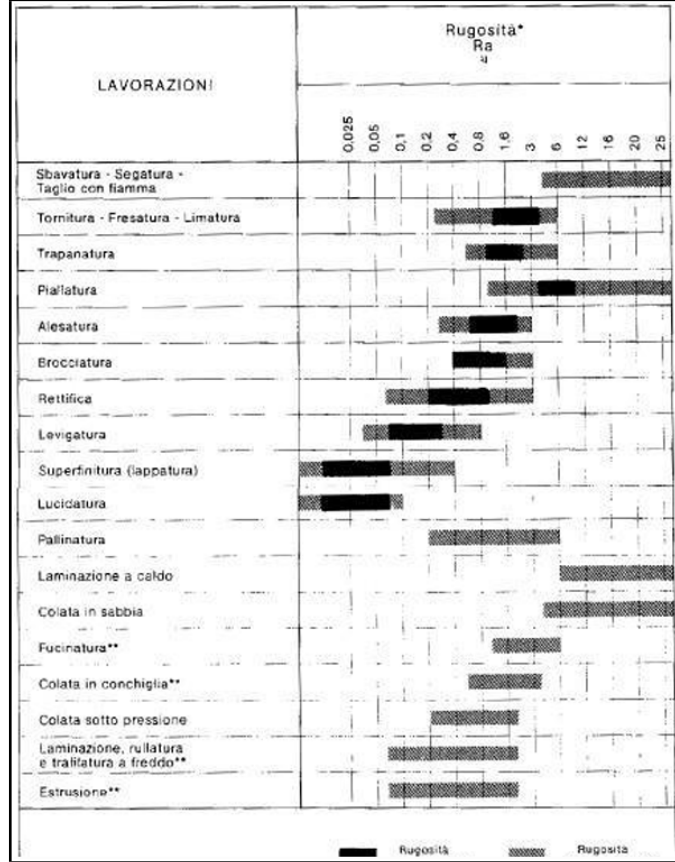


Figure 2.6: Surface Finish Factor

The first invariant  $I_{1,m}$  is computed according to its definition as superposition of principal "mean" stress components:

$$I_{1,m} = \sigma_{I,m} + \sigma_{II,m} + \sigma_{III,m} \quad (2.28)$$

The "Safety Fatigue Factor" is then calculated using the following approach:

$$\overline{\sigma_m} = \frac{N_m}{\pi \left( \left( \frac{D_e}{2} \right)^2 - \left( \frac{D_i}{2} \right)^2 \right)} \quad \overline{\sigma_a} = \frac{N_0}{\pi \left( \left( \frac{D_e}{2} \right)^2 - \left( \frac{D_i}{2} \right)^2 \right)} \quad (2.29)$$

After calculating the stress components acting on the structure the "Haigh Diagram" is used to properly assess  $\sigma_m$  influence on the fatigue limit:

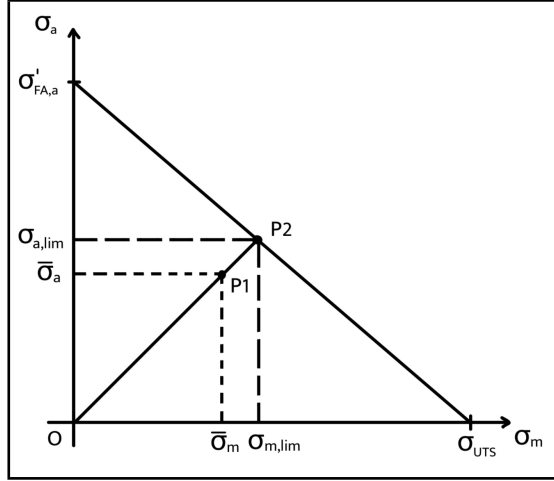


Figure 2.7: Goodman's approximation

It is used the "Goodman's line" as approximation defining the infinite life of the component, based on that and on the actual loading condition experimented by the specimen new limit conditions are evaluated:

$$\begin{cases} \sigma_{a,lim} = \sigma'_{FA,A} - \left( \frac{\sigma'_{FA,A}}{\sigma^y} \right) \sigma_{m,lim} \\ \sigma_{a,lim} = \left( \frac{\bar{\sigma}_m}{\bar{\sigma}_a} \right) \sigma_{a,lim} \end{cases}$$

$$\eta_f = \frac{\sigma_{a,lim}}{\bar{\sigma}_a} \quad (2.30)$$

By applying the definition of the Sines equivalent stress along with the previous considerations regarding the alternate principal component the criteria is now applicable:

$$\sigma_a^* = \sigma_s = \sqrt{\sigma_{I,a}^2 + \sigma_{II,a}^2 + \sigma_{III,a}^2 - \sigma_{I,a}\sigma_{II,a} - \sigma_{II,a}\sigma_{III,a} - \sigma_{I,a}\sigma_{III,a}} \quad (2.31)$$

$$\sigma_a^* \leq \sigma'_{FA,A} \left( 1 - \frac{I_{1,m}}{\sigma^y} \right) \frac{1}{\eta_f} \quad (2.32)$$

## 2.3 Application to the Specific Case

This section presents the analytical evaluation of the rotor shaft specimen under both static and fatigue loading conditions, using the material properties of 9310 VIM VAR and 32CDV13 steels. Following the methodologies introduced in the previous sections, we calculate the nominal and equivalent stresses and determine the corresponding safety factors. The comparison enables an informed material selection based on structural performance criteria.

### 2.3.1 Material Properties

The materials used in this study are two high-strength steels commonly employed in aerospace applications: 9310 VIM-VAR and 32CDV13. Their mechanical properties are considered constant, homogeneous, and representative of linear elastic behavior under the applied loads. The values used for the simulations and analytical calculations are summarized in the following table.

Material 1	9310 VIM VAR	
<b>Young modulus</b>	$E [MPa]$	200000
<b>Shear modulus</b>	$G [MPa]$	76000
<b>Poisson ratio</b>	$\nu$	0.32
<b>Yielding strength</b>	$S_{ys} [MPa]$	893
<b>Ultimate tensile strength</b>	$U_{ts} [MPa]$	1020
<b>Endurance limit</b>	$\sigma_{FA,a}[MPa]$	350

Material 2	32CDV13	
<b>Young modulus</b>	$E [MPa]$	200000
<b>Shear modulus</b>	$G [MPa]$	76000
<b>Poisson ratio</b>	$\nu$	0.3
<b>Yielding strength</b>	$S_{ys} [MPa]$	850
<b>Ultimate tensile strength</b>	$U_{ts} [MPa]$	1000
<b>Endurance limit</b>	$\sigma_{FA,a}[MPa]$	320

Figure 2.8: Mechanical properties of 9310 VIM-VAR and 32CDV13 steels.

### 2.3.2 Static Assessment of the Mast – Results

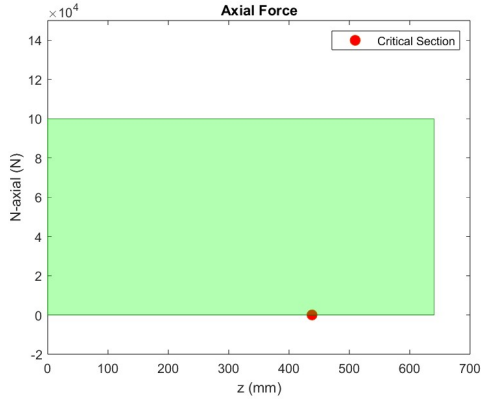
The following values summarize the outcomes of the static structural evaluation performed on the mast component at the critical section, as derived from the internal force analysis and stress computations, regarding the critical section:

- **Axial force:**  $N = 100\,000 \text{ N}$
- **Shear force:**  $T = 32\,000 \text{ N}$
- **Bending moment:**  $M_f = 41\,464 \text{ Nm}$
- **Torsional moment:**  $M_t = 80\,000 \text{ Nm}$

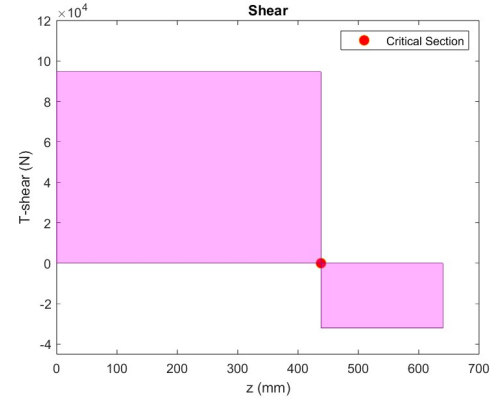
Using the section's geometric parameters:

- Internal radius:  $r_i = 70 \text{ mm}$
- Thickness:  $t = 9 \text{ mm}$

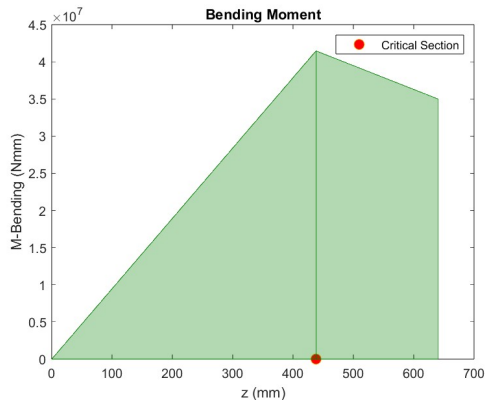
The nominal stress components at the critical section are:



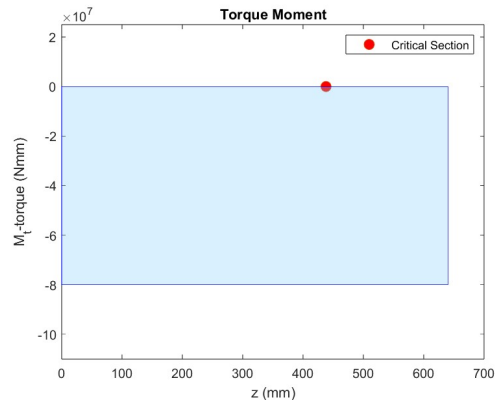
(a) Axial Force N



(b) Shear T



(c) Bending Moment M



(d) Torque Moment  $M_t$

Figure 2.9: Internal Forces Diagrams

- Axial + bending stress (nominal):  $\sigma_{\text{NOM}} = 302.898 \text{ MPa}$
- Torsional shear stress (nominal):  $\tau_{\text{NOM}} = 269.305 \text{ MPa}$

Principal stress components obtained via Mohr's circle analysis:

$$\sigma_I = 487.895 \text{ MPa}$$

$$\sigma_{II} = 0 \text{ MPa}$$

$$\sigma_{III} = -148.649 \text{ MPa}$$

Equivalent stresses according to failure criteria:

- Guest–Tresca criterion:  $\sigma_{\text{GT}}^* = \sigma_I - \sigma_{III} = 636.544 \text{ MPa}$
- Von Mises criterion:  $\sigma_{\text{VM}}^* = 576.770 \text{ MPa}$

Safety factors for the two materials:

$$\eta_1 = \frac{\sigma_1^y}{\sigma_{\text{VM}}^*} = 1.548$$

$$\eta_2 = \frac{\sigma_2^y}{\sigma_{\text{VM}}^*} = 1.474$$

These results confirm that the shaft is structurally safe under the applied static loading conditions for both 9310 VIM-VAR and 32CDV13 steels, with safety factors exceeding the unity threshold.

### 2.3.3 Static Assessment of the Specimen – Results

The results of the static structural verification conducted on the specimen, focusing on the critical section identified in correspondence with the notch, are summarized below:

- **Axial force:**  $N = 29\,000 \text{ N}$
- **Bending moment:**  $M_f = 1\,019 \text{ Nm}$
- **Torsional moment:**  $M_t = -2\,328 \text{ Nm}$

From the nominal stress contributions:

- Nominal bending stress:  $\sigma_{\text{nom}}(M_f) = 243.438 \text{ MPa}$
- Nominal axial stress:  $\sigma_{\text{nom}}(N) = 71.915 \text{ MPa}$
- Nominal torsional stress:  $\tau_{\text{nom}}(M_t) = 278.078 \text{ MPa}$

Superimposition of effects leads to:

- $\sigma_{\text{nom}} = 315.253 \text{ MPa}$

Principal stresses, obtained via Mohr's circle analysis:

$$\text{Radius} = 349.646 \text{ MPa}$$

$$\sigma_I = 477.272 \text{ MPa}$$

$$\sigma_{II} = 0 \text{ MPa}$$

$$\sigma_{III} = -162.095 \text{ MPa}$$

Equivalent stresses from the failure criteria:

- **Guest–Tresca (maximum shear):**  $\tau_{\text{MAX}} = 319.646 \text{ MPa}$
- **Von Mises:**  $\sigma_{\text{VM}}^* = 575.644 \text{ MPa}$

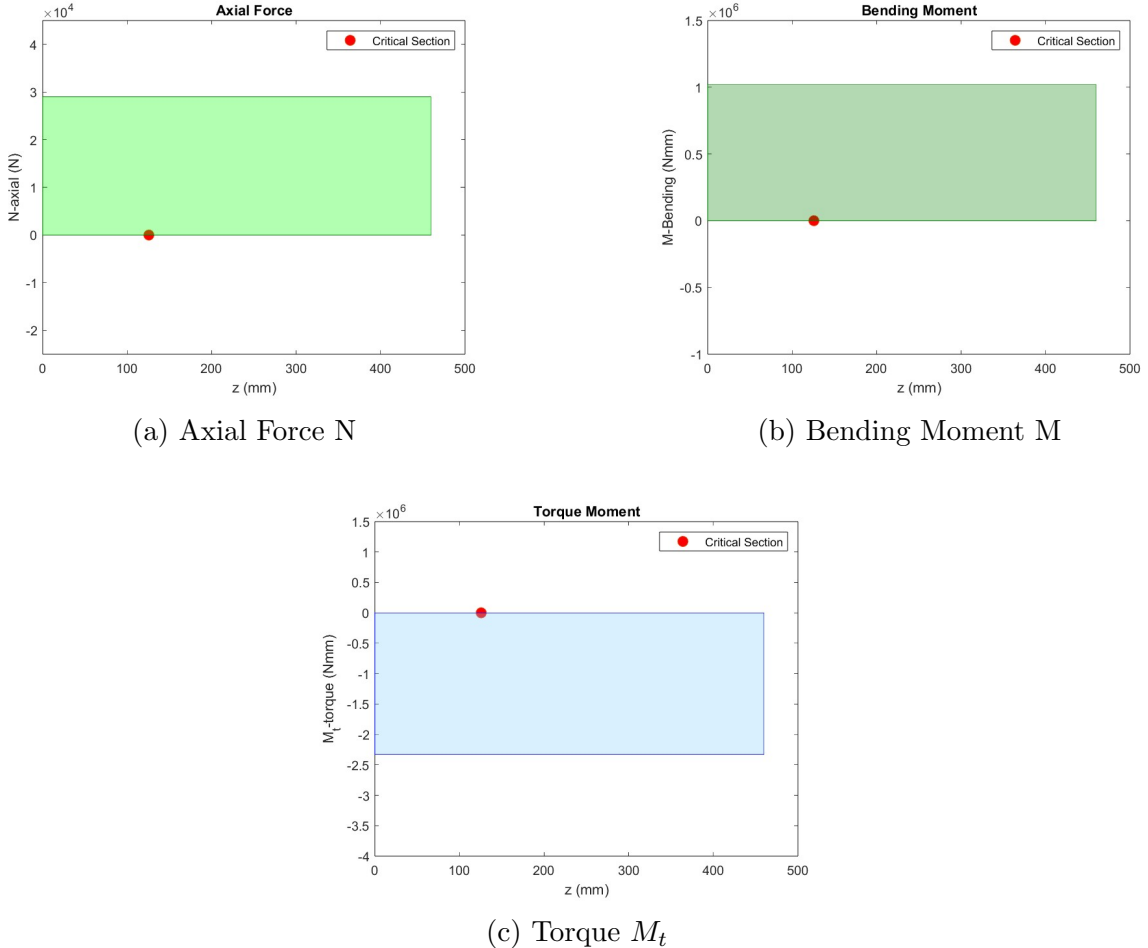


Figure 2.10: Internal Forces Diagrams

Safety factor (material 1):

$$\eta_1 = \frac{\sigma_y}{\sigma_{VM}^*} = 1.546$$

#### Stress Concentration Factor Interpolation:

To determine the stress concentration factor  $K_t$  at the notch, interpolation was performed using tabulated values from standard charts based on the geometry ratio:

- Radius-to-diameter ratio:  $r/d = 1.4913$
- Outer-to-inner diameter ratio:  $D/d = 1.0631$

Interpolating the values from the curves yielded:

$$K_t(N) = 0.92047$$

This value was then used in the correction of nominal axial stress at the notch. The bending-related  $K_t(M_F)$  had been previously interpolated as:

$$K_t(M_F) = 0.90047$$

These interpolated values were used to account for the notch effect in the stress concentration analysis.

These results confirm that the specimen satisfies static strength requirements for the given loading conditions and both materials considered, with safety margins adequately above unity.

### 2.3.4 Fatigue Assessment of the Specimen – Results

This section summarizes the results of the fatigue verification performed on the specimen, subjected to a variable axial load and constant torsional moment. The applied loading conditions are:

- **Axial force:**  $N(t) = 12\,000 + 80\,000 \cdot \sin(\omega t)$  N
- **Torsional moment:**  $M_t = 1\,500$  Nm

#### Stress evaluation:

- Mean axial stress:  $\sigma_m = 29.717$  MPa
- Alternating axial stress:  $\bar{\sigma}_a = 198.11$  MPa
- Shear stress due to torsion:  $\tau_0 = 179.174$  MPa
- Ultimate tensile strength:  $\sigma_{UTS,1} = 893$  MPa
- Ultimate tensile strength:  $\sigma_{UTS,2} = 850$  MPa
- Goodman limit estimate:  $\sigma_{a,lim,1} = 291.27$  MPa
- Goodman limit estimate:  $\sigma_{a,lim,2} = 290.55$  MPa
- $\eta_{f1} = \frac{\sigma_{a,lim,1}}{\bar{\sigma}_a} = 1.470$
- $\eta_{f2} = \frac{\sigma_{a,lim,2}}{\bar{\sigma}_a} = 1.467$

#### Sines criterion input:

- Corrected fatigue limit:  $\sigma'_{FA,a} = 306.25$  MPa
- Surface finish factor:  $m_s = 0.875$
- Geometric factor:  $m_d = 1$
- Fatigue notch factor:  $K_f = 1$

**Principal stress components (mean values):**

$$\sigma_{I,m} = 194.675 \text{ MPa}$$

$$\sigma_{II,m} = 0 \text{ MPa}$$

$$\sigma_{III,m} = -164.834 \text{ MPa}$$

**First stress invariant:**  $I_{1,m} = 29.74 \text{ MPa}$

**Sines criterion threshold (RHS):**

$$\sigma_{adm,1} = 201.367 \text{ MPa}$$

$$\sigma_{adm,2} = 201.545 \text{ MPa}$$

**Sines equivalent stress:**

$$\sigma_a^* = \bar{\sigma}_a = 198.11 \text{ MPa}$$

**Sines criterion result:** Criterion verified for both Material (1,2)

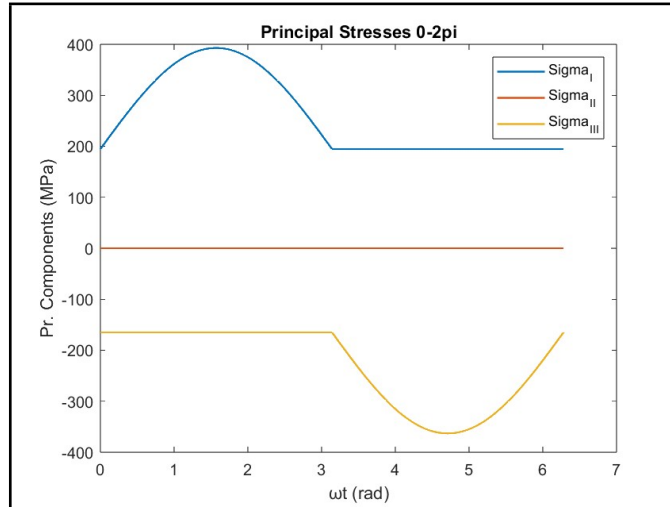


Figure 2.11: Principal Stresses Variation

**Eulerian instability check:**

- Minimum axial force:  $N_{\min} = N_m - \max(N_a) = -68\,000 \text{ N}$
- Eulerian critical load divided by safety factor:  $\frac{P_{cr}}{\eta} = 97\,239 \text{ N}$
- Stability criterion satisfied

All evaluations confirm that the specimen meets fatigue requirements under the defined alternating axial and constant torsional loads for both materials, with safety factors above unity and stability ensured against buckling.

### 2.3.5 FEM Model and Its Application

To evaluate the structural behavior of the helicopter's main rotor shaft, a Finite Element Method (FEM) analysis was carried out using **Abaqus**. The objective of the simulation was to verify the shaft's performance under both **static** and **fatigue loading conditions** and to support the analytical validation with numerical results.

#### Geometry and Simplification

The shaft was modeled as a hollow cylindrical structure with three critical regions featuring geometric discontinuities (notches), representing the most stress-concentrated areas. The CAD geometry was simplified to preserve the main stress-raising features while minimizing meshing complexity and computation time.

Two **master nodes** were introduced at the shaft ends and coupled to their respective shaft faces. These served to impose boundary conditions efficiently. One end was fully constrained (encastre), simulating a fixed support, while the other was subjected to external loading. Kinematic coupling was defined using the **continuum distributing** option in Abaqus, ensuring a smooth and physically representative load transfer over the shaft end surfaces.

The geometrical and mechanical parameters used for the analysis are reported in Figure 2.8.

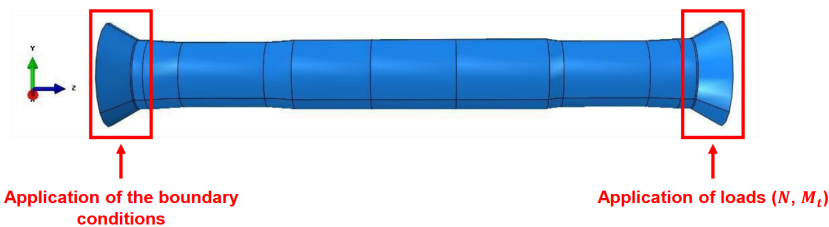


Figure 2.12: Geometry simplification and boundary condition locations

#### Boundary Conditions and Loading

##### Static case:

- Fully fixed constraint at one shaft end. 2.13
- Loading applied at the opposite end using the master node coupling:
  - Torque moment of 2328 Nm
  - Bending moment of 1019 Nm
  - Axial tensile force of 29 000 N

### Fatigue case:

- Identical constraints and coupling as in the static case.
- Time-dependent loading applied:
  - Constant torque of 1500 Nm
  - Mean axial force of 12 000 N
  - Alternating sinusoidal axial force with amplitude 80 000 N

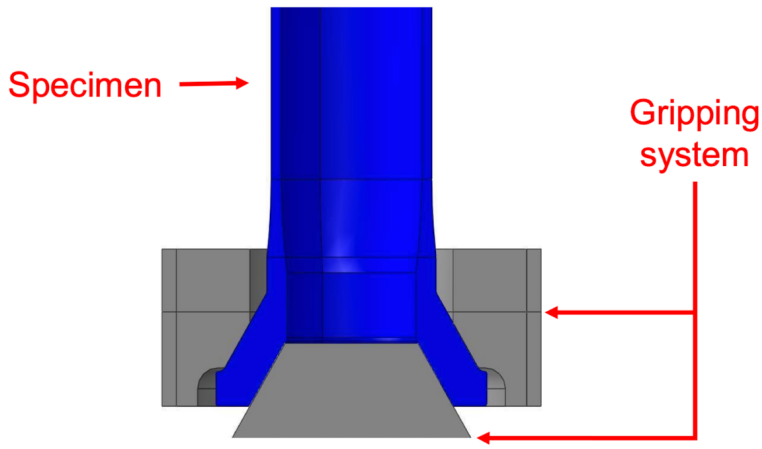


Figure 2.13: Cross-sectional view of the experimental setup

### Meshing Strategy

A structured meshing approach was adopted to ensure numerical reliability in stress concentration zones. The mesh was composed of **hex elements** with **reduced integration** and **linear geometric order** (C3D8R), ensuring efficient computation while avoiding hourglass effects. Mesh topology was structured where possible to improve element quality and minimize distortion.

After an initial coarse meshing test to identify peak stress zones, a refined mesh was applied in high-gradient regions, particularly around the inner and outer notch transitions, with element sizes down to 1 mm. Mesh consistency was verified using Abaqus's quality tools, although no full convergence study was executed.

### Results Overview and Material Comparison

Simulations were performed for both materials under investigation: **9310 VIM-VAR** and **32CDV13**. The resulting stress fields showed negligible differences between the

two cases. The maximum discrepancies in peak stress values were below the tolerance thresholds typically induced by the mesh resolution and shape function interpolation. As such, no meaningful variation was observed in the stress distribution nor in the location of critical regions.

### Static Simulation:

- Maximum Von Mises stress: approximately 571.5 MPa
- Stress localized near the inner notch transitions

### Fatigue Simulation:

- Maximum Von Mises stress: approximately 379.0 MPa
- Stress again concentrated around the same geometric discontinuities

These values align well with manual analytical predictions, supporting the validity of the simplified model and confirming that mesh and formulation errors remained within acceptable bounds.

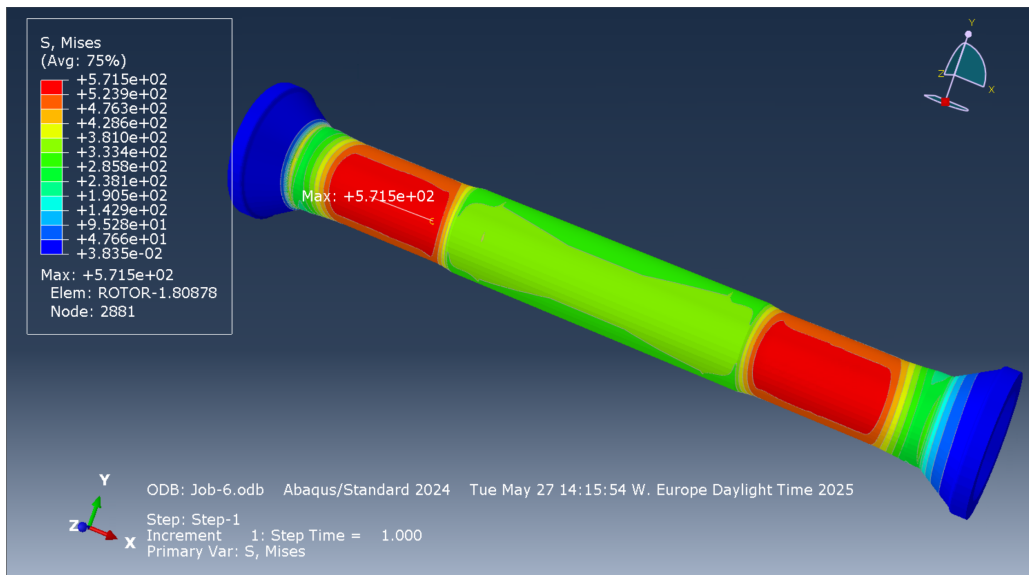


Figure 2.14: Stress distribution under static loading

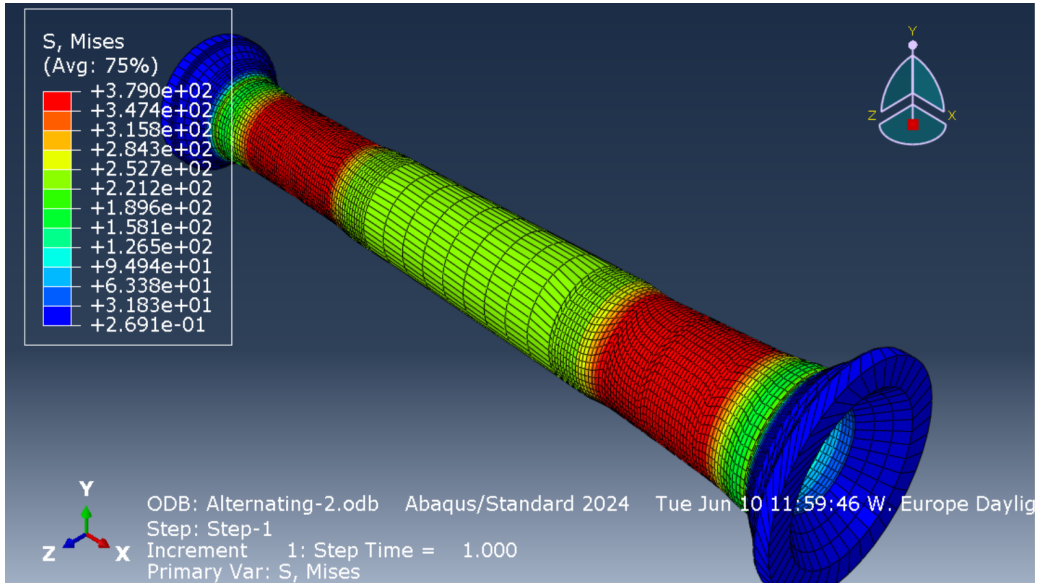


Figure 2.15: Stress distribution under fatigue (alternating) loading

## 2.4 Results and Discussions

### 2.4.1 Comparison between analytical, numerical and experimental results

A direct comparison has been carried out among the stress values obtained through the three different approaches developed in the project: the analytical formulation, the finite element simulation (FEM), and the experimental analysis based on strain gauge rosettes.

All methods refer to the same cross-section of the component, the region located at the notch, which has been identified as the most critical point from the static point of view. Therefore, the theoretical values can be directly compared to the experimental and numerical ones, without introducing artificial amplification.

The stress state in the section was reconstructed as follows:

- Analytically, from the applied loads  $N = 92 \text{ kN}$  and  $M_t = 1500 \text{ Nm}$ , assuming uniform distribution of axial and torsional stress.
- Numerically, via FEM, by evaluating the stress tensor at the location corresponding to the experimental rosettes.
- Experimentally, through tri-axial strain rosettes and the application of linear elastic constitutive laws under plane strain conditions.

Strain gauges are sensors that vary their electrical resistance with the application of a force. When an object or structure is subjected to a force, stresses and deformations are generated. The strain gauge detects and converts these deformations into a measurable

electrical signal. Three-directional strain gauge rosettes are used when the directions of the principal deformations are unknown. From the measurements of the grids in the 3 directions, by calculation, the principal directions and the deformations and stresses in these directions can be traced. Rectangular strain gauge rosettes have three measuring grids oriented at  $-45^\circ/0^\circ/45^\circ$ .

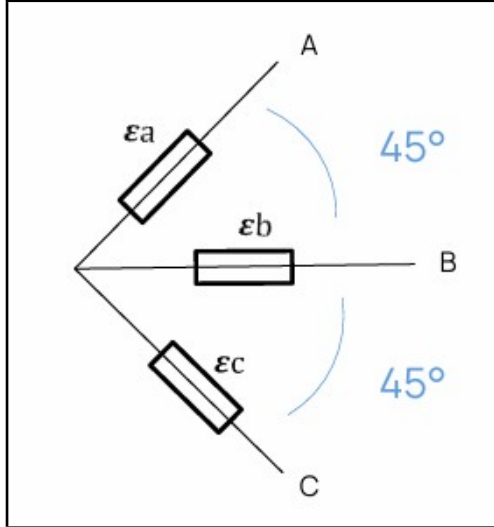


Figure 2.16: Strain gauge rosette

The table below summarizes the comparison between the three approaches in terms of the local components of the stress tensor, the equivalent Von Mises stress, and the resulting safety factor:

Table 2.1: Comparison of stress components and safety factors in the critical section at rosette number 1, for material 1 (9310 VIM-VAR) with respect to the experimental campaign A, dated 5/4/2024.

Method	$\sigma_z$ [MPa]	$\tau_{xy}$ [MPa]	$\sigma_{VM}$ [MPa]	$\eta = \sigma_{yield}/\sigma_{VM}$
Analytical	227.83	179.17	<b>384.99</b>	2.21
FEM	240.10	176.80	<b>379.00</b>	2.34
Experimental	199.18	133.78	<b>305.55</b>	2.92

The Von Mises stresses obtained through the analytical and FEM approaches show close agreement across all evaluated quantities, validating the numerical implementation and confirming the consistency of the assumed loading and boundary conditions. On the other hand, the experimental results exhibit significantly lower stress values, particularly in the principal and equivalent stress components. This discrepancy may be attributed to several factors, including partial strain transfer due to imperfect bonding of strain gauges, frictional effects in the gripping system, or slight misalignments during the load

application. Additionally, local stress gradients or stress relaxation phenomena, which are not captured by the simplified analytical model nor fully resolved by the numerical simulation, may have contributed to the observed reduction. Despite these differences, the overall comparison still supports the validity of the experimental setup, while highlighting the inherent limitations in reproducing idealized loading conditions in a real testing environment.

# Chapter 3

## Final Conclusions

This project focused on evaluating the structural behavior of a helicopter main rotor shaft under both static and fatigue loading conditions. The work combined analytical methods, finite element simulations (FEM), and experimental testing with strain gauges to get a clear and complete understanding of how the shaft performs.

### Static Assessment

In the static part of the study, we identified the most stressed section of the shaft and looked at the contributions of axial, torsional, bending, and shear loads. We also considered geometric features like notches, which can increase stress locally. Using classical formulas and stress concentration factors, we calculated the key stress components and checked them against the yield strength of two materials: 9310 VIM-VAR and 32CDV13.

The equivalent Von Mises stress was used to evaluate the safety of the component:

$$\sigma^* = \sqrt{\sigma_I^2 + \sigma_{II}^2 + \sigma_{III}^2 - \sigma_I\sigma_{II} - \sigma_{II}\sigma_{III} - \sigma_I\sigma_{III}} \quad (3.1)$$

In both cases, the resulting safety factor

$$\eta = \frac{\sigma_y}{\sigma^*} \quad (3.2)$$

was well above 1, confirming that the shaft can safely handle the given loads.

### Fatigue Assessment

For the fatigue analysis, we applied a sinusoidal axial load combined with a constant torsional moment, simulating realistic flight conditions. We split the stress into mean and

alternating parts, and used the Sines criterion to check fatigue resistance:

$$\sigma_a^* \leq \sigma'_{\text{FA,A}} \left( 1 - \frac{I_{1,m}}{\sigma_y} \right) \frac{1}{\eta_f} \quad (3.3)$$

Both materials passed this check, meaning the shaft should be able to withstand cyclic loading without failure. The results were also consistent with what we expected from the Haigh diagram (based on the Goodman line), which helped to visually confirm the fatigue limits.

## FEM Analysis

We used Abaqus to run finite element simulations, both in static and fatigue conditions. The model was simplified to reduce computation time but still included the main geometric features that affect stress distribution.

Results showed that the highest stresses were located at the inner notch transitions—exactly as predicted by the analytical calculations. For the static case, FEM returned a maximum stress of around 571.5 MPa, while for the fatigue case it was about 379.0 MPa. These values lined up well with our manual calculations.

## Experimental Validation

We measured the real stress state using strain gauge rosettes placed on the physical specimen. The experimental Von Mises stress was lower than both the analytical and FEM results (by approximately 20%), which may reflect conservative model assumptions or minor losses in strain transfer during testing. Despite the discrepancy, the experimental data trends remained consistent with expectations, supporting the validity of the modeling strategy. The consistency across all three methods (analytical, numerical, experimental) was one of the most important outcomes of this project.

## General Evaluation

The conducted analysis confirmed that the rotor shaft is structurally adequate under both static and fatigue loading conditions. Analytical and FEM-based approaches yielded closely matching results, with minor discrepancies attributable to geometric simplifications and numerical assumptions.

Both materials evaluated—9310 VIM-VAR and 32CDV13—met the design criteria in terms of strength and fatigue resistance. While 9310 VIM-VAR showed slightly higher safety margins, the differences were not structurally decisive.

In aerospace applications, where mass efficiency and cost-effectiveness are both relevant, material selection must consider factors beyond mechanical performance. 32CDV13 offers a marginally lower density ( $7.84 \text{ g/cm}^3$  vs.  $7.85 \text{ g/cm}^3$ ), which may benefit weight-sensitive systems. However, it typically incurs higher processing costs due to advanced surface treatments like nitriding. Conversely, 9310 VIM-VAR is widely available, easier to process, and more cost-effective.

Given that both materials satisfy performance requirements, the final choice should align with system-level priorities. If cost and manufacturing simplicity are preferred, 9310 VIM-VAR is the recommended option. If weight reduction or enhanced surface properties are crucial, 32CDV13 may be justified. Overall, 9310 VIM-VAR presents a slightly more balanced trade-off between performance, manufacturability, and cost.

## Future Developments and Ideas

While the project reached its main goals, there's definitely room to improve and go further with this kind of analysis. Here are some ideas for future work:

### 1. FEM Improvements

- **Mesh Convergence:** Running a full mesh convergence study would help understand how the results change with element size, and make the simulations even more accurate.
- **Contact and Friction Effects:** Adding friction and contact modeling between parts—like in the spline connection—would make the simulation more realistic.
- **Plasticity:** Including non-linear material models would let us check how the shaft behaves under overload or near-failure conditions.
- **Thermal Loads:** Simulating combined mechanical and thermal loads could help study the shaft's performance in harsh environments.

### 2. Experimental Enhancements

- **More Gauges:** Using more strain gauges on the surface would allow a better reconstruction of the full stress field.
- **Multiaxial Fatigue Testing:** Running full-scale tests with combined bending, torsion, and axial loads would give more realistic data.
- **Digital Image Correlation:** Introducing DIC could help visualize surface deformations in high detail and validate FEM results.

- **Environmental Effects:** Testing under different temperatures and humidity could reveal how the shaft behaves in real-world flight conditions.

### 3. Design Innovation and Monitoring

- **Shape Optimization:** With the stress data, we could run shape optimization algorithms to reduce weight while keeping the same safety levels.
- **Composite Materials:** Trying hybrid solutions (e.g., steel-composite shafts) could lead to better fatigue performance and lower mass.
- **Health Monitoring:** Embedding sensors (like fiber Bragg gratings) inside the shaft would allow real-time monitoring and improve reliability.
- **Probabilistic Methods:** Introducing variability in geometry and loads using Monte Carlo simulations could make the design more robust to uncertainties.

## Looking Ahead

In the long term, the goal would be to develop a modular, flexible verification method that combines theory, simulation, and testing. This could eventually support smart design and maintenance strategies based on real-time data and digital twins, especially for aerospace parts exposed to demanding loading.

## Final Thoughts

This project was a solid opportunity to apply engineering tools to a realistic component, using a combination of theory, simulation, and experiments. The workflow we followed can definitely be used as a starting point for more advanced analysis of safety-critical aerospace structures.

# Bibliography

- [1] G. D. Padfield, *Helicopter Flight Dynamics: The Theory and Application of Flying Qualities and Simulation Modelling*. John Wiley & Sons, 2008.
- [2] W. Johnson, *Helicopter Theory*. Dover Publications, 1994.
- [3] L. Castro and D. Peters, “Design of Composite Helicopter Rotor Shafts: Weight and Performance Considerations,” *Journal of the American Helicopter Society*, vol. 50, no. 3, pp. 234–245, 2005.
- [4] P. Fromme, “Structural health monitoring of composite structures using guided ultrasonic waves,” *Philosophical Transactions of the Royal Society A*, vol. 365, no. 1851, pp. 3061–3074, 2007.
- [5] MD Helicopters, “MD 500/600 Technical Overview,” Manufacturer’s Manual, 2019.  
Available: <https://www.mdhelicopters.com>
- [6] Luchsinger, “Rosette estensimetriche rettangolari a tre estensimetri,” Available: <https://www.luchsinger.it/it/sensori/deformazione/estensimetri-esa/rosette-rettangolari/>
- [7] TM’sChannel, ”ABAQUS: A Basic Introduction,” 2017, Available: [https://youtu.be/S0iBbmGw02Q?si=2RMAWvA\\_sdSXkef3](https://youtu.be/S0iBbmGw02Q?si=2RMAWvA_sdSXkef3)
- [8] ARSiTech (Formerly SimTech05) ,”Amplitude in Abaqus - Part 01 (Tabular, Equally spaced, Periodic, Modulated, smoothing on/off),” 2021, Available: [https://youtu.be/riAL3UI\\_DPk?si=o1cBYY0hMP1QTCQh](https://youtu.be/riAL3UI_DPk?si=o1cBYY0hMP1QTCQh)